~~MS0619 (2), Review & Approval Desk,~~
~~12690 for DOE/OSTI~~

SANDIA REPORT

NOV 25

SAND97–2785 • UC–704
Unlimited Release
Printed November 1997

Process Development for Electron Beam Joining of Ceramic and Glass Components

RECEIVED
DEC 0 1 1997
OSTI

B. N. Turman, S. Jill Glass, Pin Yang, Frank P. Gerstle, John A. Halbleib, Thomas E. Voth, Bonnie McKenzie, Jerry R. Clifford, Kerry Habiger

MASTER

Prepared by
Sandia National Laboratories
Albuquerque, New Mexico 87185 and Livermore, California 94550

Sandia is a multiprogram laboratory operated by Sandia Corporation, a Lockheed Martin Company, for the United States Department of Energy under Contract DE-AC04-94AL85000.

DISTRIBUTION OF THIS DOCUMENT IS UNLIMITED

Approved for public release; further dissemination unlimited.

Sandia National Laboratories

Issued by Sandia National Laboratories, operated for the United States Department of Energy by Sandia Corporation.

NOTICE: This report was prepared as an account of work sponsored by an agency of the United States Government. Neither the United States Government nor any agency thereof, nor any of their employees, nor any of their contractors, subcontractors, or their employees, makes any warranty, express or implied, or assumes any legal liability or responsibility for the accuracy, completeness, or usefulness of any information, apparatus, product, or process disclosed, or represents that its use would not infringe privately owned rights. Reference herein to any specific commercial product, process, or service by trade name, trademark, manufacturer, or otherwise, does not necessarily constitute or imply its endorsement, recommendation, or favoring by the United States Government, any agency thereof, or any of their contractors or subcontractors. The views and opinions expressed herein do not necessarily state or reflect those of the United States Government, any agency thereof, or any of their contractors.

Printed in the United States of America. This report has been reproduced directly from the best available copy.

Available to DOE and DOE contractors from
Office of Scientific and Technical Information
P.O. Box 62
Oak Ridge, TN 37831

Prices available from (615) 576-8401, FTS 626-8401

Available to the public from
National Technical Information Service
U.S. Department of Commerce
5285 Port Royal Rd
Springfield, VA 22161

NTIS price codes
Printed copy: A03
Microfiche copy: A01

DISCLAIMER

Portions of this document may be illegible in electronic image products. Images are produced from the best available original document.

SAND97-2785
Unlimited Release
Printed November 1997

Distribution
Category UC-704

PROCESS DEVELOPMENT FOR ELECTRON BEAM JOINING OF CERAMIC AND GLASS COMPONENTS

B. N. Turman
Beam Applications and Initiatives Department

S. Jill Glass
Materials Joining Department

Pin Yang, Frank P. Gerstle
Ceramic and Glass Department

John A. Halbleib
Simulation Technology Research Department

Thomas E. Voth
Thermal Sciences Department

Bonnie McKenzie
Microstructural Analysis Department

Sandia National Laboratories
P. O. Box 5800
Albuquerque, NM 87185-1182

Jerry R. Clifford, Kerry Habiger
Titan Advanced Technologies Group
Albuquerque, New Mexico 87102

Abstract

The purpose of this project is to develop and extend the electron beam joining process to applications related to Mo/Al_2O_3 cermets for neutron tube fabrication, glass seals for flat panel displays, and ceramics for structural applications. The key issue is the identification of the allowable operating ranges that produce thermal conditions favorable to robust joining and sealing. High strength, hermetic braze joints between ceramic components have been produced using high energy electron beams. With a penetration depth into a typical ceramic of ~1 cm for a 10 MeV electron beam, this method provides the capability for rapid, transient brazing operations where temperature control of heat sensitive components is essential. The method deposits energy directly into a buried joint, allowing otherwise inaccessible interfaces to be brazed. The combination of transient heating, with higher thermal conductivity, lower heat capacity, and lower melting temperature of braze metals relative to the ceramic materials, enables a pulsed high power beam to melt a braze metal without producing excessive ceramic temperatures. We have demonstrated the feasibility of this process related to ceramic coupons as well as ceramic and glass tubes and cylindrical shapes. The transient thermal response was predicted, using as input the energy absorption predicted from

the coupled electron-photon and thermal transport analysis. The joining experiments were conducted with an RF linear accelerator at 10-13 MV. The repetition rate of the pulsed beam was varied between 8 and 120 Hz, the average beam current was varied between 8 and 120 microamperes, and the power was varied up to 1.5 kW. These beam parameters gave a beam power density between 0.2 to 2 kW/cm^2. The duration of the joining runs varied from 5 to 600 sec. Joining experiments have provided high strength joints between alumina and alumina and between alumina and cermet joints in cylindrical geometry. These joints provided good hermetic seals. A series of tests was conducted to determine the minimum beam power and exposure time for producing a hermetic seal. An empirical relation has been developed, showing linear dependence of strength with exposure time, while the strength is proportional to beam power raised to the 1.5 power.

TABLE OF CONTENTS

1. Introduction

With a penetration depth of ~1 cm for a 10 MeV electron beam into a typical ceramic, electron beam joining provides the capability for directing energy into a buried, or inaccessible joint, and provides the possibility of transient brazing operations where temperature control of critical components is essential. Ceramic sealing and joining are important in the commercial and defense sectors. Ceramic insulators and power tubes are increasingly used in generation of high power electrical and microwave components. High temperatures (400-1000°C) are needed to form hermetic ceramic seals. Localized heating of the joint by an electron beam optimized for materials and geometry could open exciting possibilities, such as allowing temperature-sensitive electronic components to be assembled into sub-systems prior to brazing. The rapid braze rates that can be achieved with this process, typically a five minute total heating cycle, offer the potential of a greatly reduced process time for small-lot sealing operations. Ceramics such as Si_3N_4 and SiC are seeing increasing use for high temperature structural applications such as turbochargers for automobile engines, turbines for aircraft auxiliary power units, stator shrouds for gas turbines for power generation applications, ceramic armor, ceramic thermal protection tiles, and high energy flux mirrors. Although ceramics are being fabricated that can survive these challenging environments, their application is still limited by the lack of suitable technologies for joining them to components such as metal shafts or for joining them to themselves. A limitation of conventional joining techniques is that they require that all of the parts to be joined be exposed to high temperatures, which may degrade the performance of these components. Thus alternative joining techniques are being explored.

2. Radiation and Thermal Transport Modeling

2.1. Introduction

In this work, high-energy electron beam brazing of ceramic components was modeled numerically in order to enhance the design and operation of an experimental brazing apparatus. The transient thermal response of the part was predicted, using as input the energy absorption predicted from the coupled electron-photon transport analysis. The geometry of the experimental apparatus varied during the course of the project as modeling and experimentation indicated changes necessary to optimize the process; however, the geometry shown in Figure 1 is consistent with that used for the analyses. In all analyses, the geometry was assumed to be axisymmetric.

2.2. Numerical Model

The thermal response of the apparatus was predicted using a one-way coupled electron-photon transport/thermal analysis. Coupling of the thermal and electron-photon transport response was accomplished by first predicting the temperature independent electron-photon transport within the assembly using a Monte Carlo code. The resulting energy deposition rates were then mapped onto the finite element mesh for the thermal analysis as energy generation terms. A brief description of the numerical models is provided below:

Energy deposition resulting from electron beam irradiation was modeled by simulating the coupled electron-photon transport within the apparatus. In the present application, electron-beam energy deposition was simulated with the Integrated TIGER Series (ITS) code system.[1] The ITS system combines conventional microscopic (single scattering) Monte Carlo for photon transport with a macroscopic random walk technique for electron transport.[2] Coupling of the two species is complete in the sense that the physical model includes all relevant processes for the production of photons by electrons and the production of electrons by photons. In addition to elastic scattering, electrons and positrons can produce knock-on electrons, bremsstrahlung photons, annihilation radiation, and fluorescence photons and Auger electrons following electron/positron impact ionization. In addition to coherent (elastic) scattering, photons can produce electrons via incoherent scattering, electron-positron

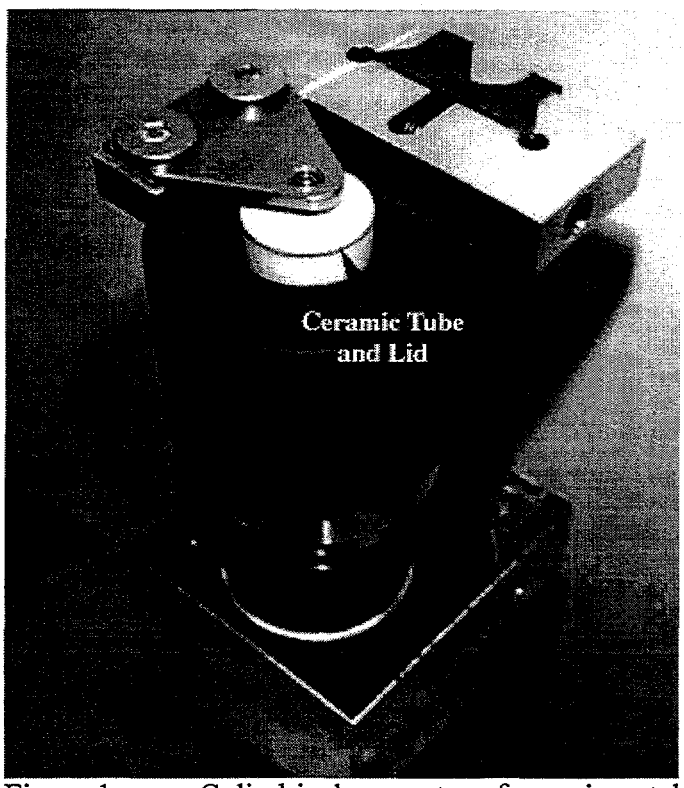

Figure 1 Cylindrical geometry of experimental apparatus.

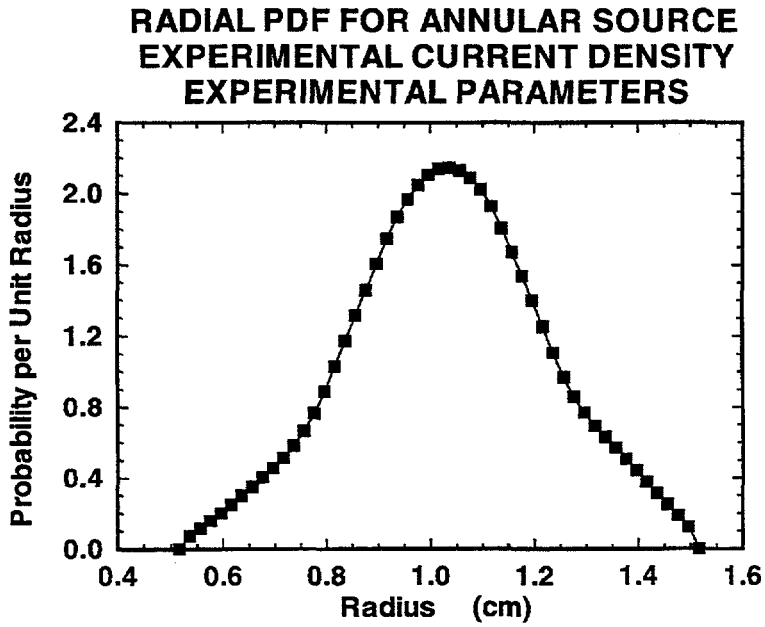

Figure 2 Effective annular distribution of electron beam source, for rotating cylinder.

pairs via the pair-production interaction, and photoelectrons, fluorescence photons, and Auger electrons through photoelectric absorption.[1]

The axisymmetric CYLTRAN code of the ITS system was employed to simulate two-dimensional spatial profiles of the beam power deposition throughout the apparatus for the cylindrical brazing experiments. The axisymmetric distribution of the source beam, approximately centered on the spinning cylindrical wall, was modeled as an annular source of monoenergetic, 10 MeV electrons, normally incident to the part lid (see Figure 1). The annular distribution of the source is plotted in Figure 2. The remaining boundaries are specified as non-reentrant (i.e., electrons leaving the electron-photon transport computational domain are lost).

Thermal transport was assumed to be governed by the thermal diffusion equation, with temperature independent density and thermal conductivity. Specific heat was assumed constant for all materials except the braze. Braze specific heat was assumed to vary, with an increased value between the liquidus and solidus temperatures to account for latent heat effects during melting. Thermal boundary conditions were typically assumed to be radiative from exposed surfaces while convective losses were assumed negligible as the experiments simulated were performed in a vacuum. The thermal analysis was performed using COYOTE II,[3] which is a finite element code for solving the non-linear heat diffusion equation. Energy deposition rates calculated by the electron-photon transport code were mapped to the finite element quadrature points using a code developed for this project and the USRVHS.f routine in the COYOTE II user subroutine library.

2.3. Modeling Results for Ceramic and Glass Tubes and Lids

A large number of simulations were performed during the course of this project to define the thermal and radiation parameters for the problem. Parametric simulations for a range of beam currents were performed in addition to variations in thermal boundary conditions and apparatus, braze and part materials in order to optimize the experimental apparatus and process. An overall summary of the results is provided in the following.

In order to estimate the penetrating power of the 10-MeV beam for various apparatus components, numerous one-dimensional radiation transport simulations were performed using the TIGER code of the ITS system. Of particular importance were depth profiles in the various lid materials to ensure that the magnitude and uniformity of the deposition in the vicinity of the braze would be adequate. Figure 3 is an example of such a profile in alumina ceramic. It shows that alumina lids with thickness greater than about 0.8 cm could prevent adequate penetration of a 10-MeV beam.

Once the beam profile and lid thickness were defined, simulations were performed to optimize the thermal response of the system. Specifically, the initial apparatus design incorporated only a thin layer of thermal insulation between the ceramic part and base plate and provided no insulation for radiative thermal losses. Numerical simulations indicated that with this design, a beam current of 60 μA (the upper limit of beam current possible with the accelerator used in the experiments) was required to heat the braze to its melting temperature. As a result, the fixturing was revised to add more thermal insulation as well as add a radiation shield around the ceramic part. With the added insulation and radiation shield, the predicted current requirement was found to be about 20 μA, or 200 watts beam power.

Both ceramic and glass parts were considered in the analyses. The time to liquidus temperature, plus 50° C, is shown in Figure 4, as a function of beam current for both ceramic and glass tubes. These results are presented in a non-dimensional scaling relation in Figure 5, in which the dimensionless time, Fo, is related to the dimensionless beam current, i, by the following relation:

$$Fo = ta/h^2 = 170 i^{-1.31} \quad (1)$$

where

$$i = (I_b E_k / V_b)/(k_s (T_p - T_i))$$

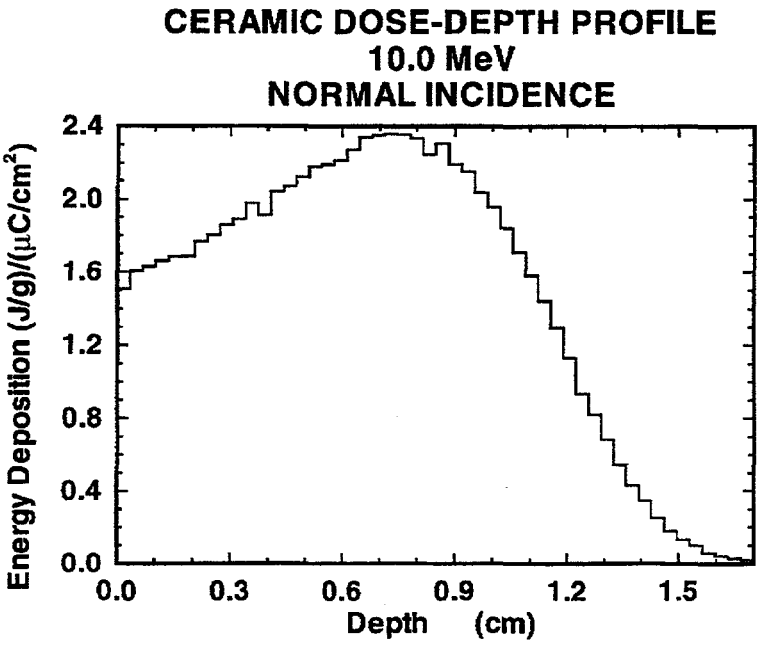

Figure 3 One-dimensional calculation of energy deposition profile.

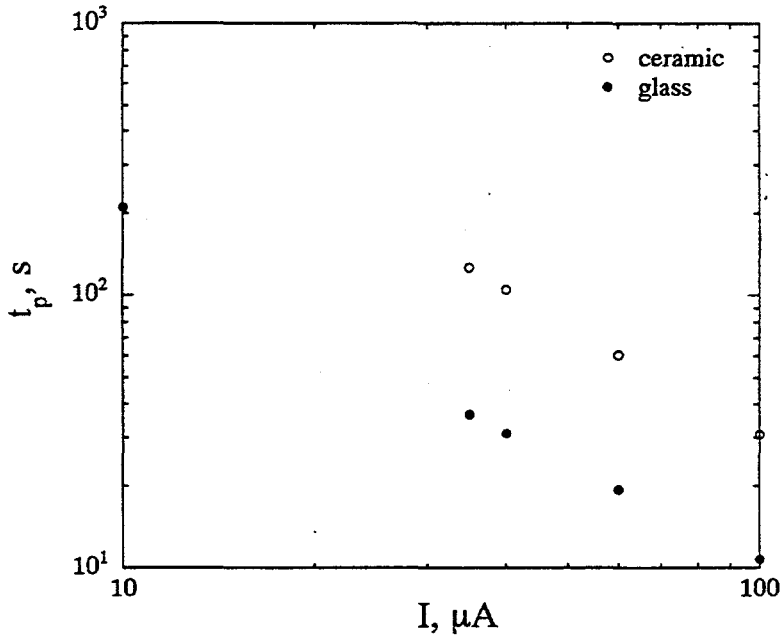

Figure 4 Process time versus beam current for ceramic and glass parts.

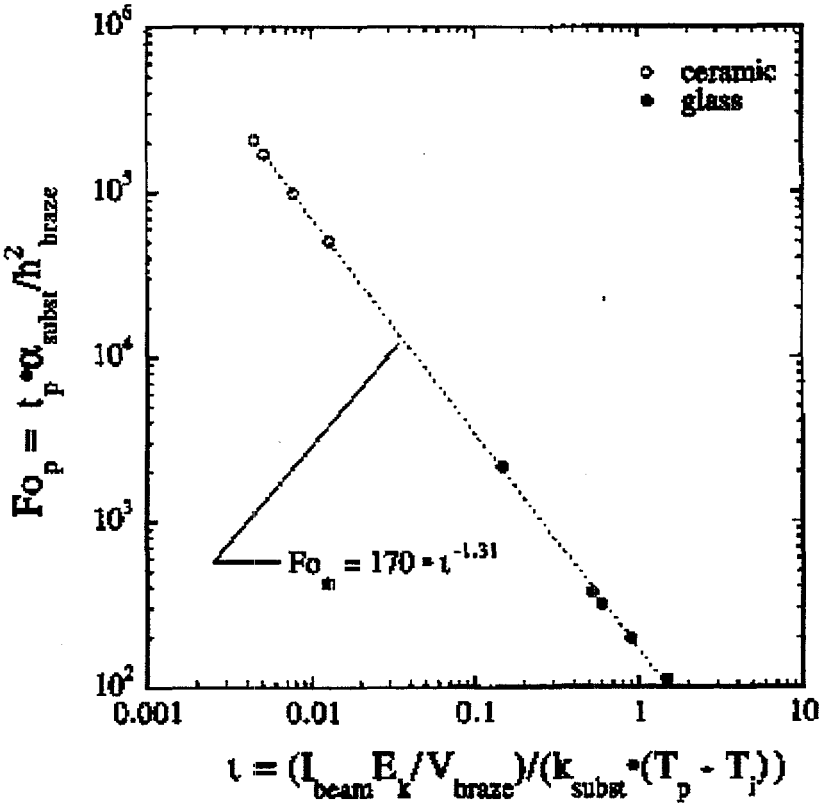

Figure 5. Non-dimensional scaling of process time and beam current, from simulations.

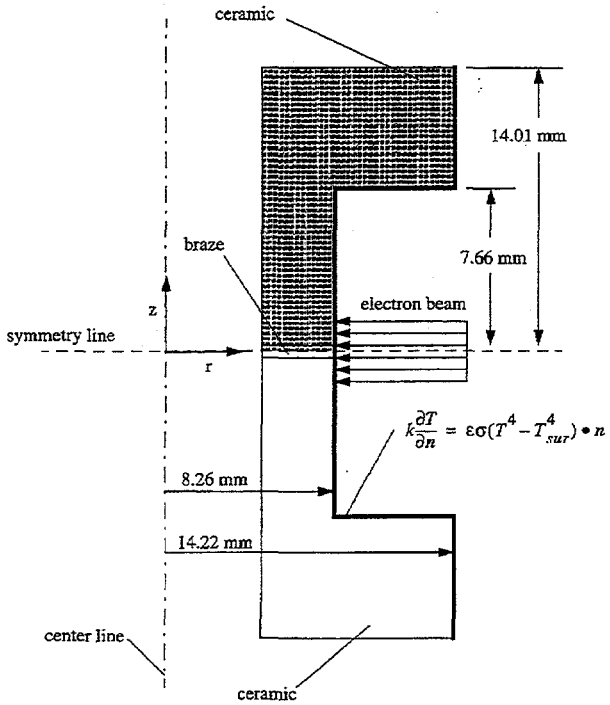

Figure 6. Schematic of the experimental test geometry for the tensile samples. The shaded region indicates the domain used for the thermal analysis.

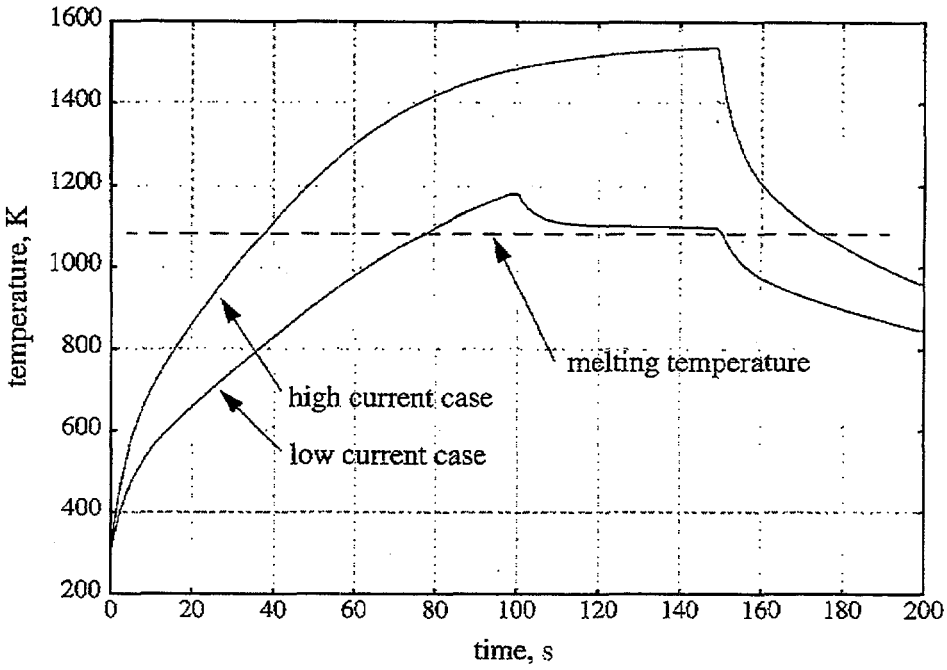

Figure 7. Braze thermal history for low and high power beam cases. Braze liquidus temperature for Cusil ABA is noted in the figure as "melting temperature."

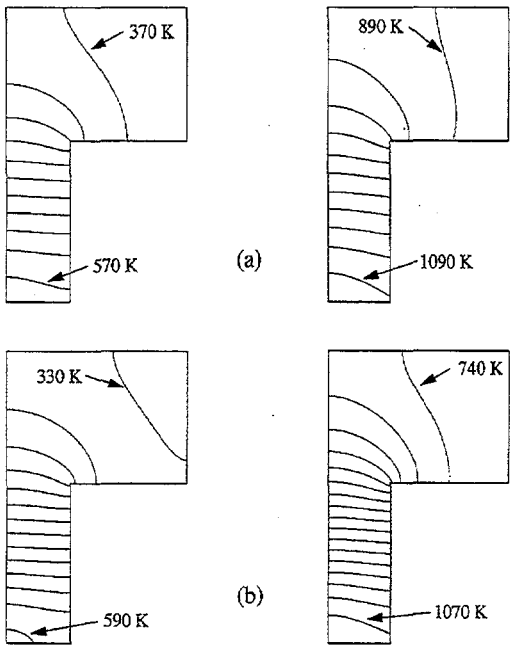

Figure 8. Ceramic component isotherm distributions for early time (15% of the melting time; left hand side) and at melting (right hand side) for a) the low beam power case, and b) the high power case. Minimum and maximum isotherms are indicated and increments are 20 K.

V_b, is the braze volume, t is time, h is the braze thickness, I_b is the beam current, E_k is the beam kinetic energy, k_s is the tube and lid's thermal conductivity, a is the thermal diffusivity of the braze, $T_p = T_m + 50°$ C, and T_m and T_i are the liquidus and initial temperatures respectively. This relation should prove useful in future electron beam brazing work as it provides a simple method to calculate possible braze melting time. Of course, caution should be exercised when using Equation 1 as it was developed for a specific part geometry and material properties. Results obtained from the equation should be taken only as a guide with detailed modeling required for accurate results.

2.4. Thermal Response Modeling of the Ceramic Tensile Strength Specimen

Modeling of the experimental tensile strength specimens has been conducted to predict the temperature profiles and evaluate the optimal power profiles. Figure 6 shows the model geometry for this analysis. In this case, the beam is incident on the sample at the equator, centered on the braze region. Because the brazing is done in vacuum, radiative transport is the only loss mechanism from the part. Radiative loss was modeled as gray diffuse, with braze and ceramic emissivities assumed to be 0.1 and 0.8 respectively. All other boundaries are assumed to be insulated.

Figure 7 shows the thermal response history of the braze material for a low beam power profile and a high beam power profile. The high beam power case is a constant at 840 watts for the entire process time. The low power case starts with 532 watts until the braze melt temperature is reached, and then it is reduced to 280 watts for the remainder of the process. Although high heating rates may be advantageous from the standpoint of process time, these high rates can produce large thermal gradients that are beyond the stress limit of the ceramic. Thus, there is an upper limit on the power and thermal gradient that can be used. The low power profile in Figure 7 was found to give a proper balance between rapid processing and tolerable temperature gradients. This profile allows the sample to reach braze melt quickly, but maintains the peak temperature to values only slightly above braze melting point. Figure 8 shows the thermal gradients associated with these runs. Figure 8 (a) is for the low power profile, and Figure 8 (b) is for the high power case. The left hand side shows the temperature gradient at 15 percent of the melting time, and the right hand side is the gradient at melt temperature. The lower power profile, and minor changes to it, were found experimentally to give good joint strength, while avoiding thermal stress cracking that was apparent with excessive temperature. For instance, for the high power case, the peak temperature reaches about 1500 K, and these experimental samples showed severe thermal cracks. The lower power profiles did not crack. More discussion of the thermal stress limits is presented in section 4.7.

3. Electron Beam Joining Experiments and Hardware

Fifty eight ceramic tensile strength/sealing specimens, twenty-one ceramic tubes, thirty-five ceramic coupon combinations, and nineteen Pyrex glass tubes were joined using a matrix of beam power and exposure time settings to identify successful operating ranges. The substrate and joining materials, and their melting points and compositions, are included in the Appendix. The quality of the joint was evaluated based on appearance, hermeticity, and strength. The descriptions of these evaluations can be found in Section 4.

Three specimen geometries were tested. The first consisted of two square coupons with approximate dimensions of 1 cm x 1 cm x 0.4 cm. Joining was conducted by placing the joining material between the two coupons on the 1 cm x 1 cm face. The samples were stationary and the beam axis was perpendicular to the 1 cm x 1 cm face of the coupons. The second joining geometry consisted of cylindrical tubes with circular discs for lids. The tubes had an outside diameter of 2.54 cm and a wall thickness of 0.3 cm, and length of approximately 2.54 cm. The lids were 2.54 cm in diameter and varied in thickness from 1-2 mm for the alumina, 1.5 mm for the cermet, and 3 mm for the Pyrex glass. The braze thickness was typically 75 μm, although a thicker, 250 μm Ticusil braze was also used for a few tests. The third geometry was used for tensile testing, and consisted of two funnel-shaped alumina pieces brazed together at the narrow end to form an hour-glass shape (see Figure 6). The specimen was rotated under the electron beam, which was aligned perpendicular to the braze joint.

The joining experiments were conducted with the Titan RF Linac accelerator at 10-13 MV. The repetition rate of the pulsed beam was varied between 8 and 120 Hz, the average beam current was varied between 8

and 120 microamps, and the power was varied up to 1.5 kW. These beam parameters gave a beam power density between 0.2 to 2 kW/cm^2. The duration of the joining runs varied from 5 to 563 sec. Most experiments were run at a vacuum of less than 1 mtorr, and the pressure was less than 100 mtorr for all tests.

A rotating fixture was designed and fabricated for sealing glass tubes and lids, and alumina tubes and alumina and cermet lids. The electron beam from the Titan 10 MeV Linac was aligned so that the area to be joined was uniformly heated around the circumference as the part rotated under the beam at a speed of 1000 rpm or 16 rpm. To reduce thermal loss, the rotating fixture included a radiation shield and thermal insulation (Coors R-38) between the ceramic tube and the base plate.

4. Joint Evaluations

4.1. Introduction

Representative samples from most of the materials combinations and sets of joining conditions have been examined and tested. Optical and scanning electron microscopy (SEM) were used to evaluate melting and wetting of the bonding materials, and to evaluate the degree of reaction between the braze metals and the ceramic substrates. The mechanical integrity of coupon and cylinder joints has been evaluated using shear strength tests. Prior to shear testing or sectioning for microstructural examination, some samples were examined non-destructively using ultrasound to evaluate the degree of bonding in the joint area.

4.2. Hermeticity Testing

Hermeticity tests were conducted on tube and lid joint samples, using a helium leak test at a vacuum level of 10^{-9} torr as the standard. The results of these tests are included in Section 4.7. A series of tests with alumina tubes and tensile samples were conducted to evaluate the range of power required for hermetic sealing. The results showed the upper and lower power limits, dictated by thermal stress-induced microcracking at the upper end, and braze melting at the lower end (see Figure 21). Ten of the thirteen Pyrex tubes sealed with the Schott glass frit were hermetic. All three of the Pyrex tubes joined with the Johnson Matthey frit leaked at a rate $>10^{-5}$/cc He/sec, even though the glass appeared to have melted and bonded. Section 4.8 (Figure 23) gives the glass tube hermeticity data as a function of beam power.

4.3. Optical Examination

As-joined coupon and cylinder samples were examined optically to determine if braze and frit melting had occurred during exposure to the electron beam. Low magnification observations could in most cases be used to confirm that melting had or had not occurred; however, because of the non-uniformity of the beam, braze material in one region of the joint may have melted while regions farther from the beam center may have remained unmelted. Thus observation of the outside of the joined specimens may not have been sufficient to reveal whether melting occurred in the specimen interior if the beam were misaligned relative to the center of the specimen.

Because of the transparency of the glass samples, regions where melting occurred were easier to distinguish. Unmelted vs. melted regions of the Schott frit in the same joint are shown in Figure 9. Although optical examination of Pyrex cylinders bonded with glass frit showed that frit melting had occurred, optical observations alone were not sufficient to determine why a particular sample was or was not hermetic. Microcracking, or very small scale irregularities, may be responsible for leaks at very low or very high power levels.

4.4. Ultrasonic Examination

Ultrasound was used to obtain a non-destructive qualitative picture of bonding of coupon specimens prior to sectioning or shear testing. The ability to determine the quality of the bond is based on the principle that well-bonded regions do not produce as strong a return signal as those that are weakly bonded or unbonded. Exams of coupon samples indicated that bonding is generally uniform, although there were unbonded

regions. This may be due to the fact that in some cases the braze was not completely flat prior to melting and there was insufficient applied pressure to flatten it. Non-uniform bonding may also occur due to the non-uniformity of the beam. This can lead to high temperatures at the beam center and decreasing temperatures as a function of distance from the beam center. Examples of well-bonded and poorly-bonded specimens are shown in Figures 10 and 11.

4.5. Scanning Electron Microscopy (SEM) Examination

Joined specimens were sectioned and polished using standard metallographic preparation techniques. SEM examinations revealed that with the appropriate electron beam power and exposure parameters, melting, wetting, and bonding of the joint material "appears" to have occurred for each of the materials combinations. The difficulty with evaluating the true behavior of the braze materials using sectioned and polished samples is that the braze materials are quite soft relative to the substrate materials and can be smeared into the substrate surface.

SEM examination showed why some cermet lids bonded to alumina tubes were not hermetic. Figure 12 of sample A6 shows that although the Cusil ABA braze has melted, its coverage of the cermet and alumina is not uniform and it is not adhering completely to either material along the length of the joint cross-section. This sample was from the first group of tubes joined when the vacuum was insufficient and braze oxidation appeared excessive. A much better bond is shown in the SEM micrograph in Figure 13. Uniform joint coverage has been achieved and a close-up of the joint in Figure 14 shows a thin Ti-rich reaction layer between the braze and both adjoining materials.

Figures 15 and 16 show the Ticusil braze joint for two alumina joints. The braze appearance is more homogeneous in Figure 16 than in Figure 15 and this is consistent with optical observation of the sample, which indicated that the braze had not fully melted. Figure 16 also shows evidence of a Ti-rich reaction layer between the braze and the alumina which would indicate that the braze was hot enough to melt and react with the alumina substrate.

Figure 17 shows the Ticusil braze for the cermet joint. This figure shows a reaction layer between the braze and the adjacent substrate materials that promotes bonding between the braze and these materials. Figure 18 shows a Nioro braze joint between cermet and alumina. Although there is no evidence of a reaction layer between the braze and the substrate materials, in some regions of the braze joint there is segregation of the gray phase (vanadium and nickel rich) to the cermet side of the joint. This behavior may be related to how hot the braze became in some regions. Optical observation of the outside surface of these coupons showed that very little or no melting of the braze had occurred. Much higher temperatures are required to melt the Nioro ABA braze because of its higher melting point (960°C).

SEM examination of glass frit bonded cylinders was useful in elucidating why some samples were not hermetic. For G3, which was hermetic to 10^{-9} cc He/sec, but was not expected to be based on the optical exam results, SEM revealed that it contained large bubbles, but they appeared to be isolated from one another. Conversely, for sample G4, which was not hermetic, but appeared to be well bonded based on the results of an optical exam, SEM showed that the glass contained numerous small pores that may have been connected across the joint producing a continuous leak path. Sample G-4 was processed for a longer time than G3, and thus the melted frit had longer to fill in the small pores.

4.6. Joint Strength Testing

The joint shear strength was tested by placing coupon or cylindrical samples in a 4340 steel fixture with shims to achieve very close tolerances. The top coupon or the circular lid were then pushed off in displacement control, at a rate of 0.01 mm/sec. The shear stress at failure and the cross-sectional area of the joint were used to calculate the joint shear strength. In many instances the joint may have been stronger than the measured shear strength, because the adjoining material failed, not the joint. Thus the strength results provide a lower bound for the joint shear strength. Results of these tests are given in Tables A.2 and A.3. Not all of the specimens were tested because some were used for SEM examination and some were archived. Some of the large strength variability that was observed may have been due to the

difficulty of fixturing the samples. Both pieces were not always perfectly aligned and this may have produced local stress concentrations and bending stresses in the substrate and joint that contributed to their failure during shear testing.

4.6.1. Shear Strength of Coupon Specimens

Electron beam brazing was conducted with four brazes: Cusil ABA (melt temperature 815 ^{0}C), Ticusil (850 ^{0}C), Incusil ABA (715 ^{0}C), and Easy Flo 45 (618 ^{0}C). Cusil ABA appeared to give the best results based on its melting, wetting behavior, joint appearance, and properties of the joints. The use of Ti (1.75%) as an active element in this braze alloy helps promote wetting of the alumina surfaces and reactive bonding by the braze. At vacuum pressure higher than a few millitorr, we observed significant oxidation problems with Ticusil, which has the highest Ti content and is thus most susceptible to oxidation. Below 1 millitorr, we observed no evidence of oxidation. The higher melting point of Ticusil ABA caused some cracking of the ceramic due to thermal shock. Microcracking of the braze and non-uniform reactions were observed with Incusil ABA braze. Easy Flo 45, without a reactive component, did not form a reaction layer. Therefore, Cusil ABA was used as the braze of choice for most of these experiments with alumina.

Shear strength tests indicated that most of the joints had good mechanical integrity, with the exception of the SiC-SiC joints. Strengths ranged between 88 MPa (12.7 kpsi) for Si_3N_4- Si_3N_4 coupons bonded with Ticusil and 220 MPa (31.9 kpsi) for Al_2O_3- Al_2O_3 coupons bonded with Ticusil. The strongest Si_3N_4 - Si_3N_4 bonds were produced with Ticusil braze and silicon-coated Si_3N_4 surfaces. The strength in this case was in excess of 185 MPa, the limit of testing for the shear strength test fixture. Cermet on alumina samples also produced high strengths in the range of 170-180 MPa with both Ticusil and Nioro ABA brazes. Table 1 gives the strength measurements for these materials, ignoring the effect of braze choice. To first order, the choice of braze material appears to have limited effect within the statistical error of the experiment. Ultrasound results indicated poor contact of SiC-SiC coupons bonded with Ticusil.

Table 1
Summary of Coupon Sample Shear Strength

Ceramic Material	Number of Samples	Mean Shear Strength (MPa)	Standard Dev. (MPa)	Std. Dev/Mean
Silicon Nitride	9	152	43	0.28
Silicon Carbide	3	57	20	0.34
Alumina	3	192	20	0.10

4.6.2. Shear Strength of Cylinders with Circular Lids

Strengths of six Pyrex cylinders bonded to circular lids with Schott glass frit ranged between 5.3 MPa (769 psi) and 10.1 MPa (1459 psi). The average was 7.8 ±2.1 MPa (1125±300 psi). This favorably with the strengths of three conventionally bonded joints that had an average shear strength of 5.8 ±2.2 MPa (844±312 psi).

The average strength of cermet lids bonded to alumina cylinders with Cusil ABA braze was 81.1 ±22.5 MPa (11.8 ±3.3 ksi). This compares favorably with the tensile strengths of cermet-Kovar joints bonded conventionally with Nioro ABA braze, which are typically in the range of 7-15 MPa (1 - 2.2 ksi); however, caution is necessary when comparing shear strengths to tensile strengths because of the differences in the stress state and the fixturing.

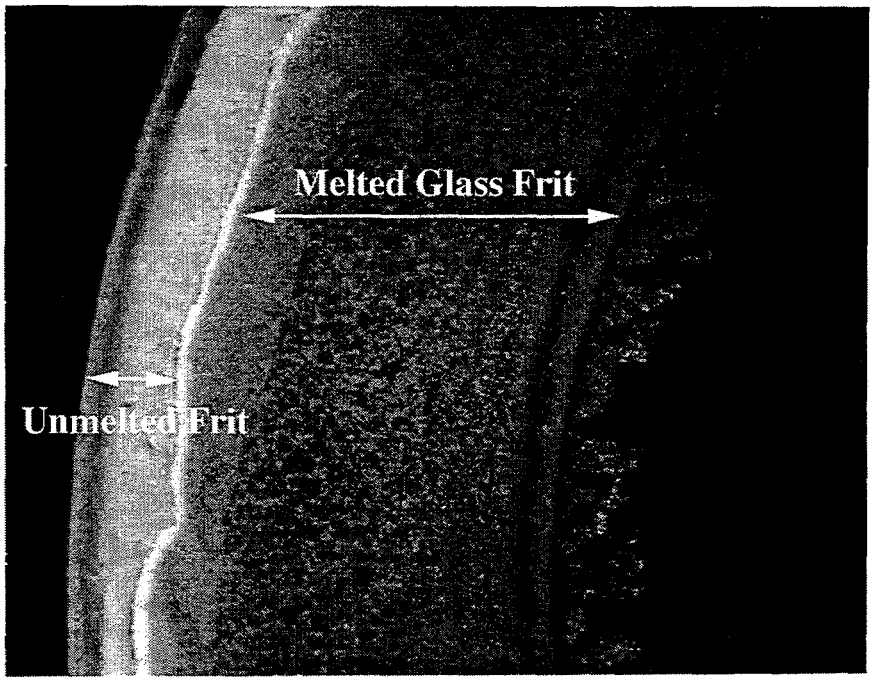

Figure 9 Optical micrograph of the top view through a Pyrex glass lid of a Schott glass frit joint. Unmelted and melted regions of the frit are shown. This seal was not hermetic.

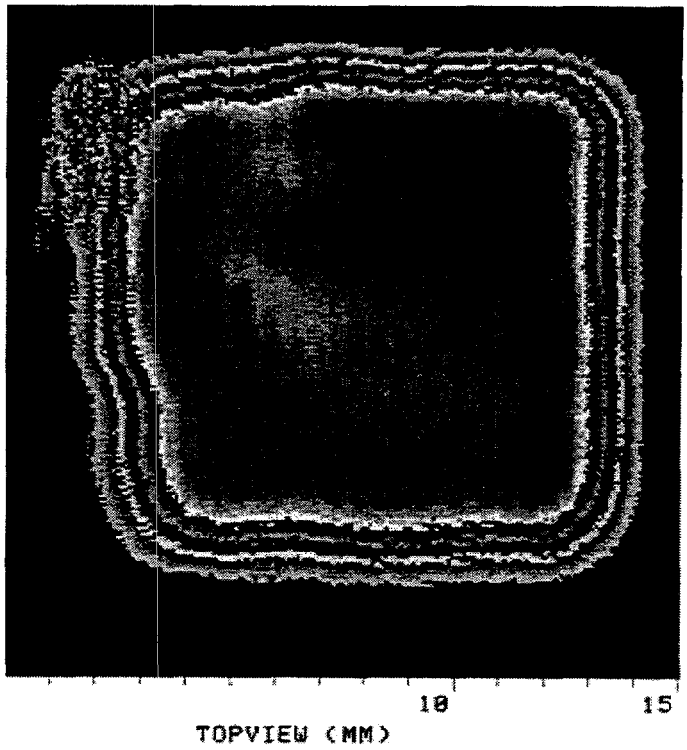

Figure 10 Ultrasonic scan through two coupons of Si_3N_4 bonded with Ticusil braze. The uniformity of the ultrasonic image indicates the uniformity of the bonding. The strength of the bonding decreases from the center to the outer edges.

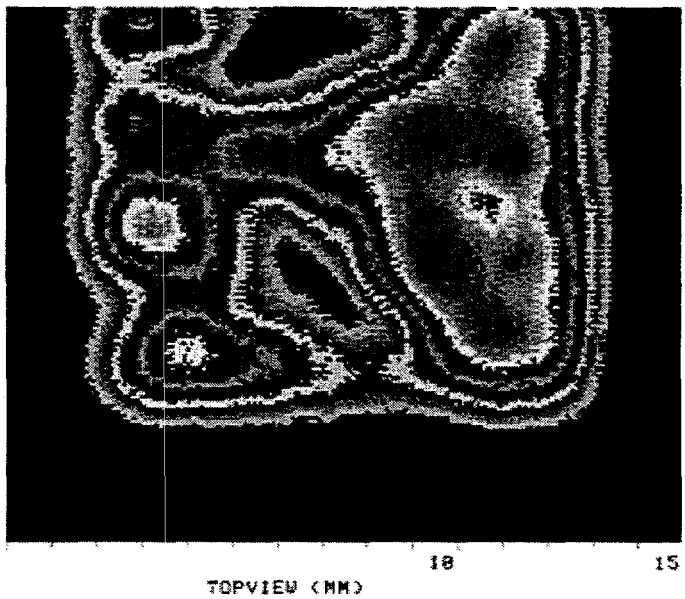

Figure 11 Ultrasonic scan through two coupons of Si_3N_4 bonded with Ticusil braze. The nonuniformity of the ultrasonic image indicates that the bonding is non-uniform. Black regions indicate complete lack of bonding.

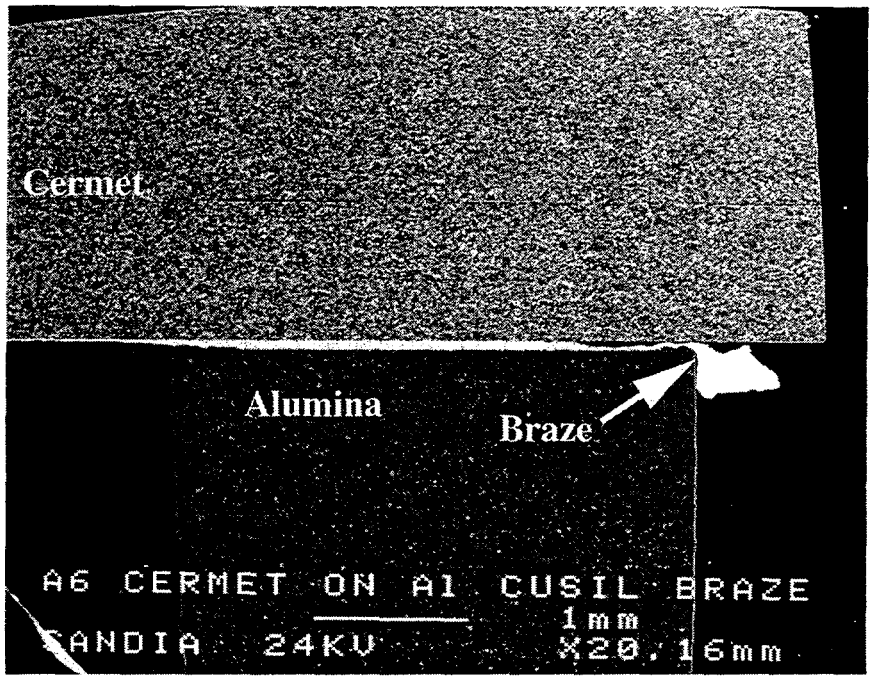

Figure 12 Scanning electron micrograph of the Cusil ABA braze interface between cermet and alumina materials. The braze, although it appears to have melted, does not form a complete bond with the adjoining cermet and alumina.

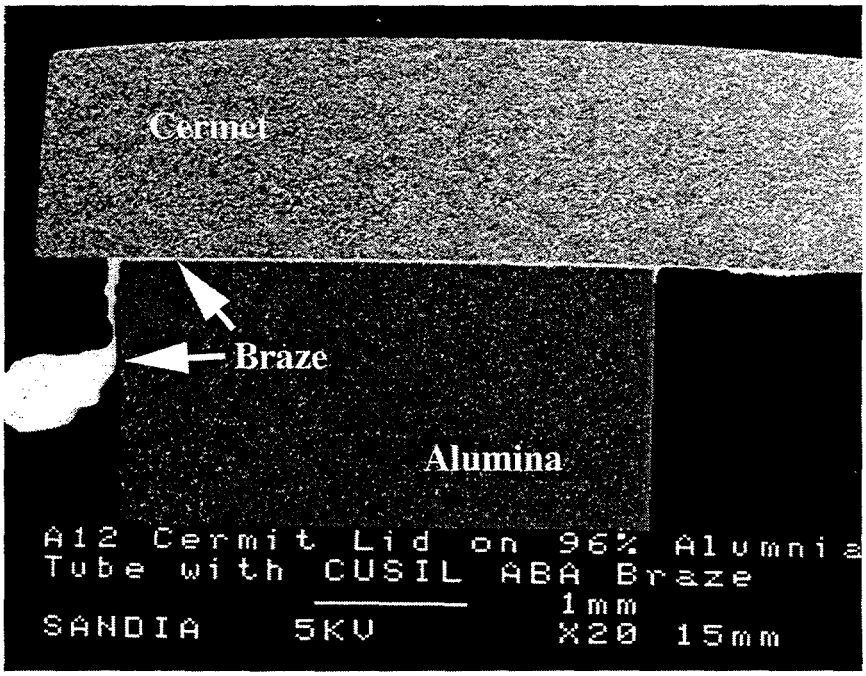

Figure 13 A more complete bond has formed between the Cusil ABA braze and the adjoining cermet and alumina compared to Fig. 12. This may be an indication that there was better melting of the braze.

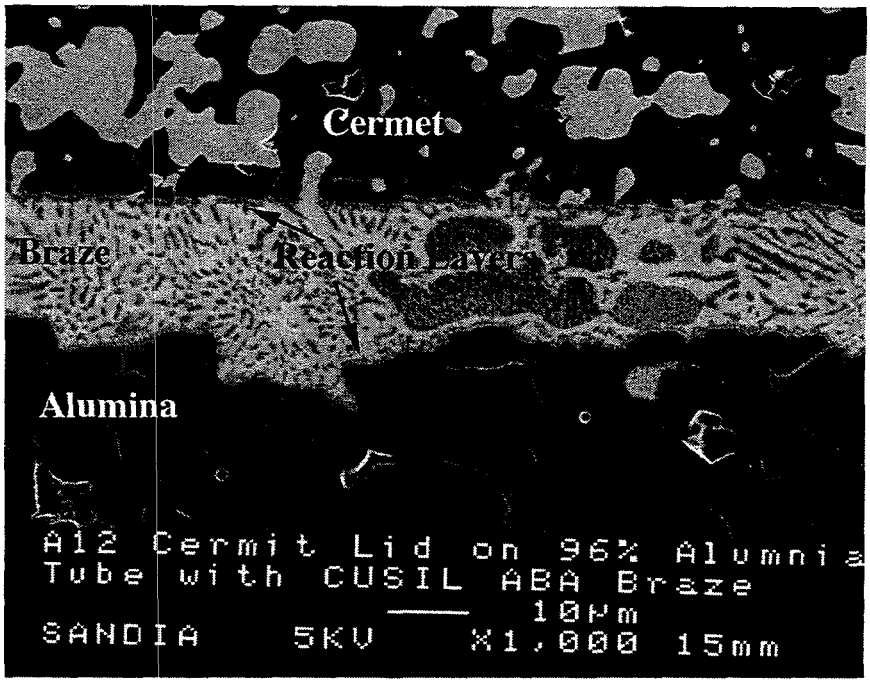

Figure 14 A higher magnification SEM micrograph of the Cusil ABA braze joint shown in Fig. 13. There is a thin reaction layer between the braze and the adjoining materials that is Ti rich.

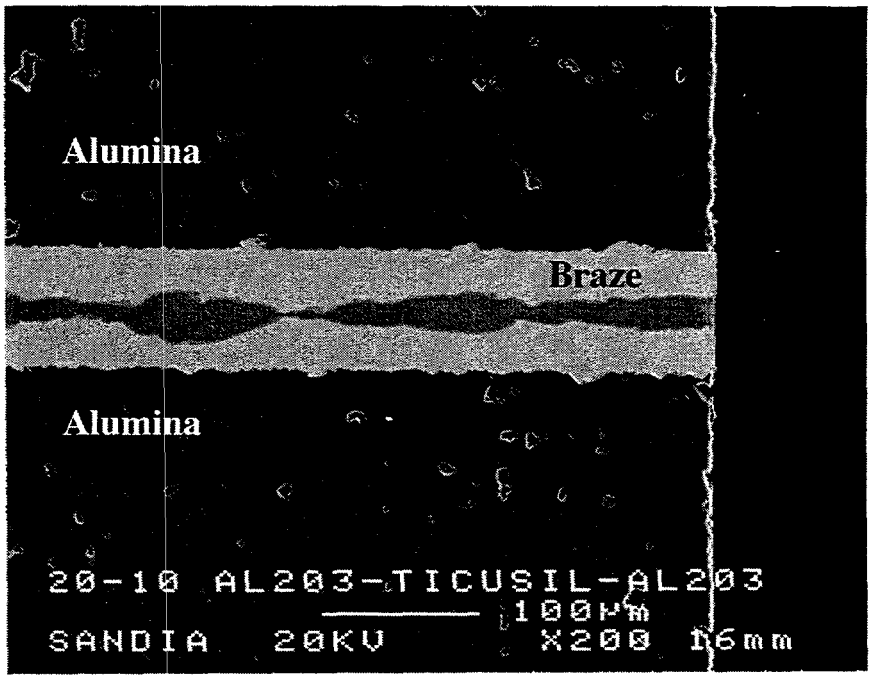

Figure 15 SEM micrograph of an alumina to alumina joint with a Ticusil braze. The large gray regions in the braze indicate that it may not have melted fully.

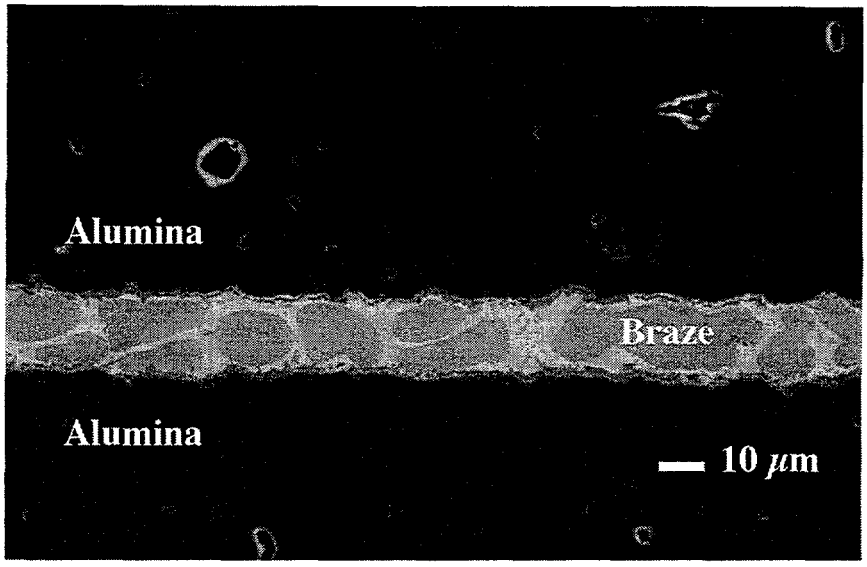

Figure 16 SEM micrograph of an alumina to alumina joint with a Ticusil braze. The distribution of the gray regions in the braze indicate that it probably reached a higher temperature than the braze in Fig. 17. There is also a thin gray region at the interface between the braze and the adjoining materials that is a Ti-rich reaction layer.

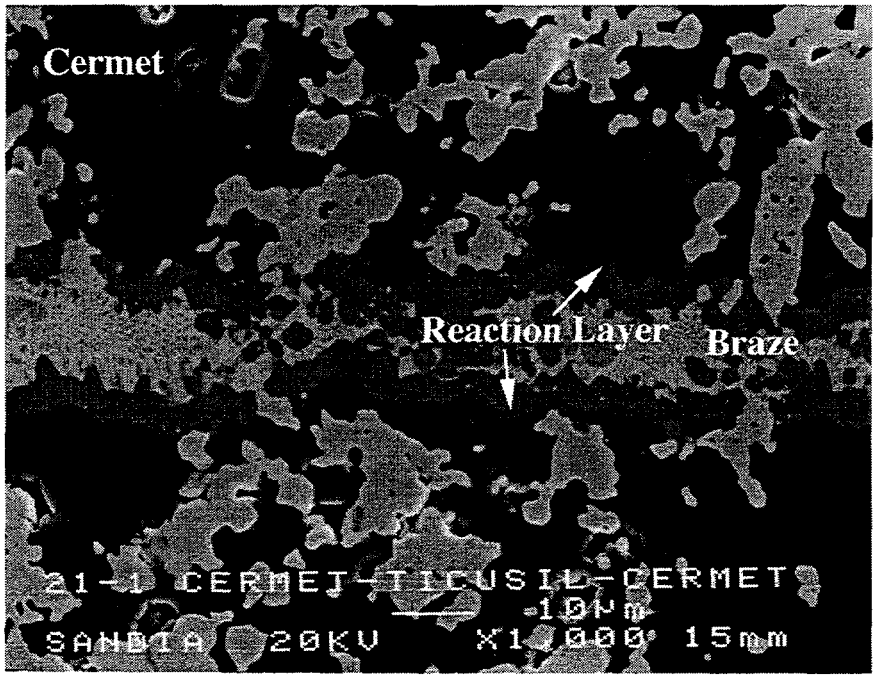

Figure 17 SEM micrograph of the Ticusil braze joint between two cermet coupons. There is a Ti-rich reaction layer at the braze-cermet interface.

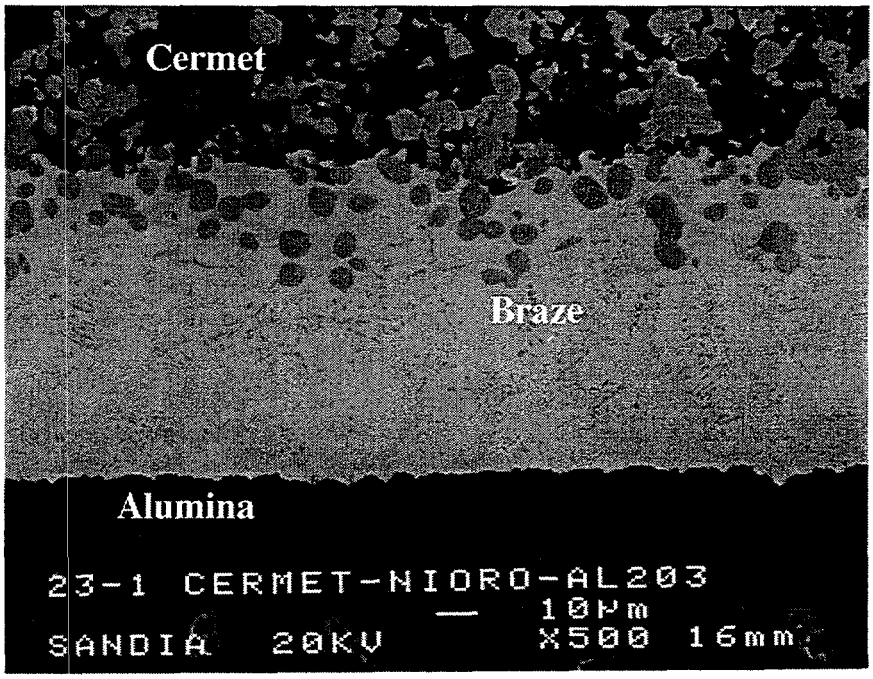

Figure 18 SEM micrograph of the Nioro ABA braze between coupons of cermet and alumina. There is segregation of the vanadium and nickel-rich phase of the braze to the cermet interface.

4.6.3. Tensile Strength with Cylindrical Pull Test Samples

Tensile strength measurements employed an ASTM standard geometry.[4] For this test, an hour-glass shaped sample was produced by joining two funnel-shaped ceramic sections at the middle, with a joint diameter of 1.6 cm. The sample was then pulled until fracture occurred. The results of those tensile tests are given in Figures 19 and 20. Two sets of experiments are shown in the figure. The first is at 840 watts beam power, approximately the maximum power at which alumina can be joined without inducing thermal shock. Tensile strength is seen to increase rapidly with increased process time. The second sample set was operated with an initial beam power of 530 watts, until the braze melt temperature was reached (100 seconds). The beam power was then reduced to 280 watts, maintaining the temperature at the melt point for the remainder of the process. This approach avoided overheating the ceramic, while providing time to form the reaction zone. The plot indicates that longer time is needed to develop the reaction zone, on the order of 600 seconds to reach the strength range of 100 MPa. We also conducted experiments with a conventional oven braze process, in which the sample was held constant at the braze melt temperature for 600 seconds. The average strength in that case was 98 MPa, consistent with the extrapolation of strength vs. process time for the low power electron beam processing.

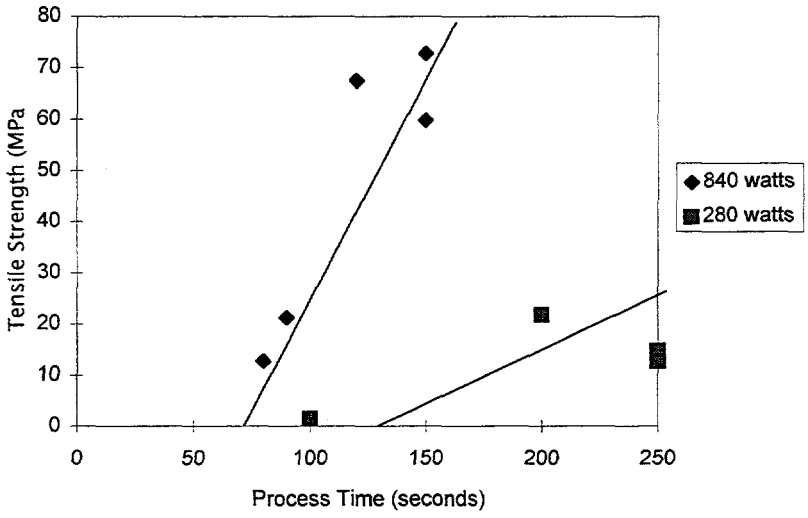

Figure 19 Tensile strength of alumina-Cusil ABA-alumina ceramic samples in a "tensile button" test configuration 5.

A total of 46 sample strength measurements have been made, with a range of beam power from 280 to 840 watts, and a range of process times from 80 to 555 seconds. We observed the melt time for these experiments with video camera monitoring. We fit these data with an empirical formula which gives a good comparison to the measured strength data. The tensile strength, in MPa, for CuSil ABA braze and the alumina tensile button geometry, is given by the formula:

$$S = 2.41 \times 10^{-5} (t - t_m) P_2^{1.5}, \qquad (2)$$

$$t_m = 2.5 \times 10^{4} / (P_1 - 250) \qquad (3)$$

P_1 = beam power during braze melting phase,
P_2 = average beam power after braze has melted.

Figure 20 shows the quality of the data fit for the 46 strength tests with CuSil ABA and the alumina tensile button samples. The measured strength, divided by $P_2^{1.5}$, is plotted against $t - t_m$. The slope of this curve

is the scaling constant of 2.41 x 10^{-5}. Measured and calculated points are correlated with a 0.93 correlation coefficient, and a standard deviation in the y-axis of 0.0014, showing excellent repeatability and fit to the data.

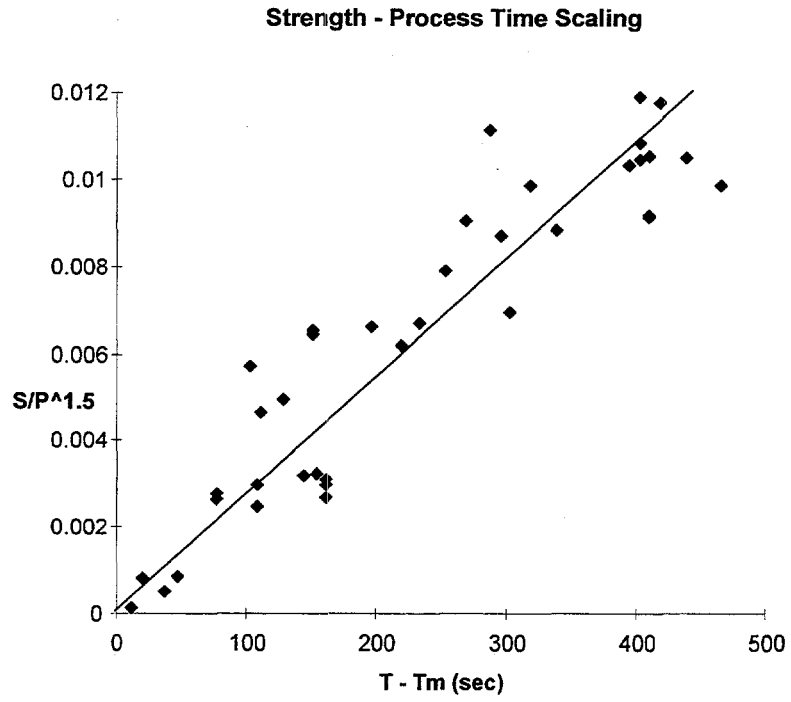

Figure 20. Measured tensile strength scaled with beam power and process time, as given in Equation 2.

4.7. Alumina Pull Test Sample Sealing Data

Hermeticity, or the ability of the sample to maintain a vacuum, was measured for each of the cylindrical pull samples, using a helium leak detector at 10^{-9} torr vacuum. These seal data are shown in Figure 21, where the beam power and process time are plotted for samples that were hermetic, shown by squares, and those that were not hermetic, shown as diamonds. Those samples with power exceeding the upper curve on Figure 21 were damaged by thermal stress cracking in the braze region and in the ceramic, and were thus prone to leaks. Below the upper curve, thermal stress cracking was not observed. A lower limit to hermetic sealing is given by the lower curve on Figure 21, which represents the melting point limit for these samples (Equation 1). The available processing window for these samples, in this geometry, is thus given by the region between the two curves. This processing window is determined by the specific thermal and mechanical limits of the material and the fixture-beam geometry, and should be determined for each specific processing situation.

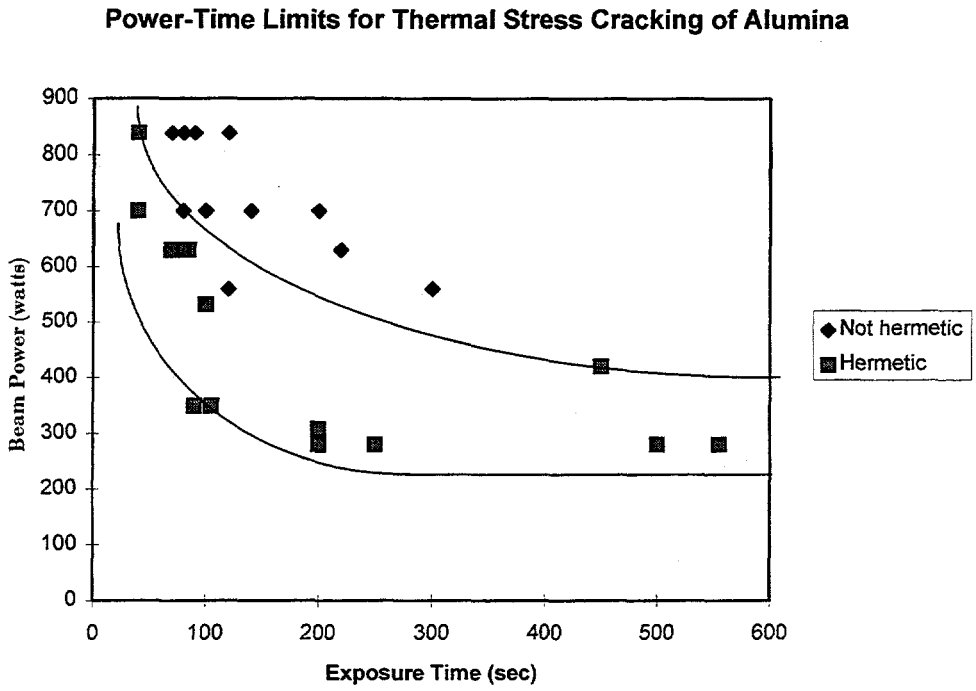

Figure 21 Hermeticity data for the cylindrical alumina pull test samples. The upper curve is the thermal stress limit for the joint, and the lower curve is the melt limit for the braze. The acceptable operating range for hermetic sealing lies between these limits.

Ultrasound transmission was used to obtain a non-destructive picture of the joint. The quality of the bond is determined by the principle that well-bonded regions transmit the ultrasonic signal more effectively (or have a lower impedance) than those that are weakly bonded. The microstructures of these joints were studied, placing special attention on the differences between "strong" and "weak" bond regions. In general, we found that regions with a "strong" bond exhibited a thicker reaction layer with a coarser eutectic microstructure in the braze, as shown in Figure 22. Development of a reaction layer, like most chemical reactions, depends on the processing temperature and time. This immediately suggests that a combination of sufficient processing temperature and reaction time is essential to develop a thick reaction layer for good bonding. Comparing the active brazing alloys, Cusil ABA seems to work best with the e-beam joining process and yields the best hermeticity and bond strength. The reaction layer was found to be much thinner for Incusil ABA than for Cusil ABA, and Incusil ABA tended to form microcracks in the braze material.

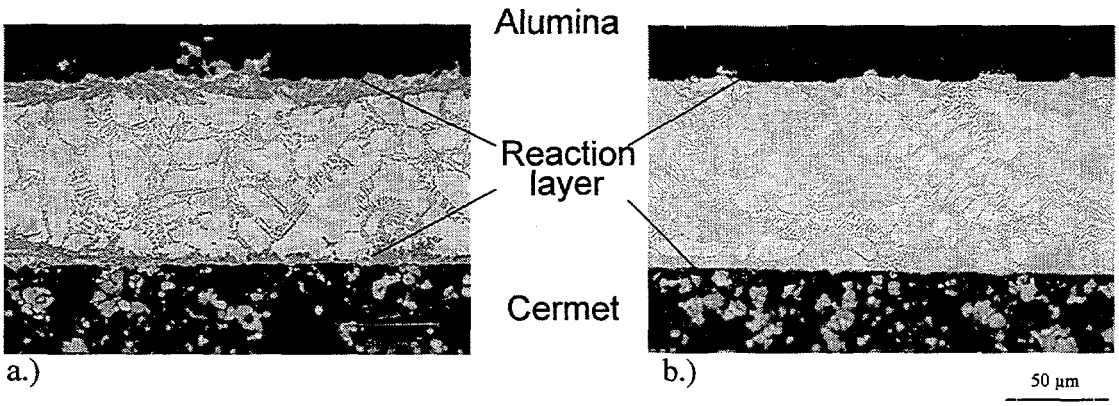

Figure 22 Scanning Electron Micrograph (SEM) cross-section through an alumina-Cusil ABA-Alumina braze joint: (a) strong, hermetic joint, and (b) weak, non-hermetic joint.

4.8. Pyrex Glass Tube Sealing

The e-beam experiments conducted with Pyrex glass tubes and lids are also shown in Table A.2 (G-series). During heating we were able to see phase changes in the Schott glass frit using a remote video camera, and could record the time at which the frit melted and wetted the lid surface. We were concerned that too rapid heating or cooling would lead to cracking, but this was only observed for one sample. Temperature ramp rates of 300°C/min and radiative cool-down rates of some 100 °C/min of the sample were sufficiently slow that cracking due to stresses caused by thermal gradients was not observed upon heating and cool-down, even when the beam power was turned off abruptly at the end of the run.

The glass sealing data are plotted in Figure 23, where the experimental processing time is plotted against beam repetition rate, showing the minimum time required to obtain hermetic seals. Samples that were hermetically sealed are shown as diamonds, and those not sealed are plotted as squares. The processing time required to produce good seals is shorter as the beam repetition rate increases. For a given beam repetition rate, shorter times are required to produce hermetic seals for the lower melting temperature glass frit than for the higher melting temperature brazes.

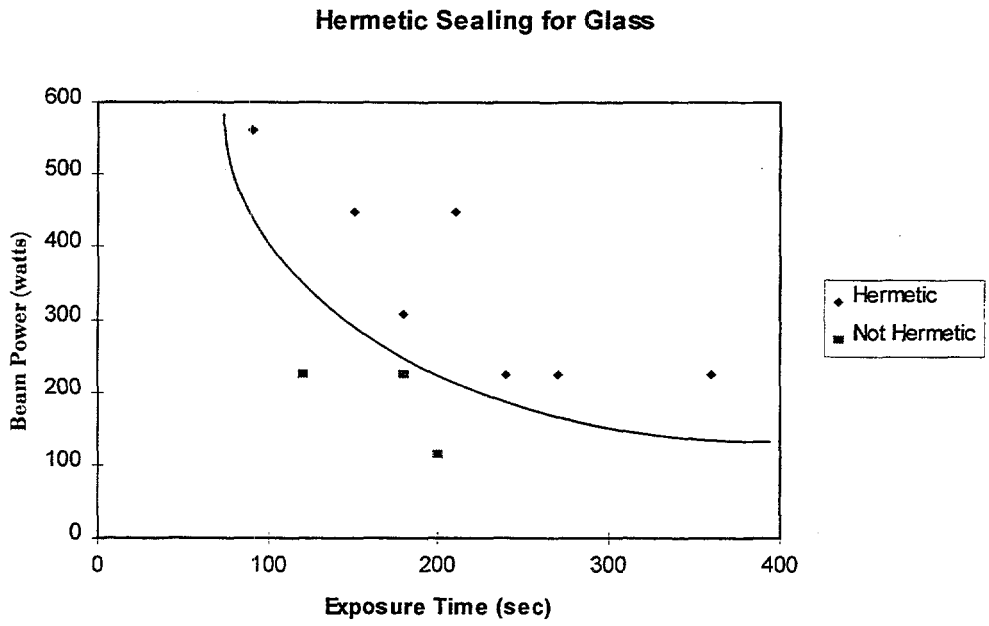

Figure 23. Sealing data for glass tubes and lids.

5. Summary

We have successfully joined and sealed ceramic tubes, demonstrating the feasibility of deep penetration electron beam joining with 10 MeV electrons. Joining experiments have provided high strength joints between alumina - alumina, and alumina - cermet in cylindrical geometry. Joint strengths of up to 118 MPa (17.1 kpsi) were measured. Square coupon samples were also joined and tested for shear strength. Shear strengths of over 200 MPa (29.0 kpsi) were measured for Si_3N_4 - Si_3N_4 and Al_2O_3 - Al_2O_3 samples. Hermetic seals between tubes and lids of alumina - alumina, alumina - cermet have been obtained. A series of tests was conducted to determine the minimum beam power and exposure time for producing a hermetic seal. An empirical relation was developed to predict the joint strength for cylindrical joints, as a function of beam power and process time. That relation, given in Equation 2, shows that the strength is related to the 1.5 exponent of beam power, and linearly with exposure time after braze melt. Thermal stress cracking

was found to be an important limiting factor for hermetic sealing, and the upper limit for power and processing time for the geometry of the alumina pull strength samples, are given in Figure 21. Beam deposition and thermal modeling was used to evaluate temperature distributions and thermal limits. The modeling results showed good agreement with experimental results.

APPENDIX

Table A.1. Joining materials used in electron beam joining experiments.

Material	Prod. Desig.	Supplier	Composition (wt% unless otherwise noted)	Melting Temperature (°C)[$]
Ceramic substrates				
Si_3N_4	AS800	Allied Signal	Si_3N_4 + proprietary sintering aids	
SiC	Hexaloy	Carborundum		
Al_2O_3		Vesuvius-McDanel	96wt % Al_2O_3, 4 wt% glass sintering aids	
Mo- Al_2O_3 cermet	CND50	Sandia (Roger Moore)	27 vol% Mo, 83 vol% of 94% Al_2O_3 (6 wt% glass)	
Metal substrate				
Kovar		Sandia neutron tube part		
Brazes for ceramic joining				
	Easy Flo 45	Handy-Harmon	15.0% Cu, 16.0% Zn, 24.0% Cd, 45.0% Ag	618°C (1145°F)
	Incusil ABA[#]	Wesgo[*]	1.25% Ti, 12.5% In, 27.25% Cu, 59.0% Ag	715°C
	Cusil ABA	Wesgo	1.75% Ti, 35.25% Cu, 63% Ag	815°C
	Ticusil	Wesgo	4.5% Ti, 26.7% Cu, 68.8% Ag	850°C
	Nioro ABA	Wesgo	15.5% Ni, 82% Au, 1.75% V, 0.75 Mo	960°C
Glass substrates				
Pyrex Glass	7740	Corning	2% Al_2O_3, 4% Na_2O_3, 13% B_2O_3, 81% SiO_2	
High PbO frit	Replaces Schott G017-334	Schott via Plasmaco	Assumed 60% PbO, 40% SiO_2 based on 4.8 g/cc density	T_{soft}=425°C
	Experimental	Johnson Matthey	Proprietary	T_m~325°C

[$] The melting temperature is the liquidus temperature for braze alloys.

[#] ABA= active braze alloy

[*] Wesgo Technical Ceramics and metals, 477 Harbour Blvd., Belmont, CA 940002

Table A.2.
Experimental Conditions and Properties for Glass and Ceramic Tube Joints

Sample	Rate (Hz)	Time (sec)	Substrate & Join Material	Comments	Shear Strength (MPa)
G-1	8	200	Pyrex, Schott glass frit	Unmelted, Too low power, not Hermetic	
G-2	16	120	Pyrex, Schott glass frit	Bonded, not Hermetic	
G-3	16	270	Pyrex, Schott glass frit	Bonded, Hermetic	
G-4	16	180	Pyrex, Schott glass frit	Bonded, Not Hermetic	
G-5	16	240	Pyrex, Schott glass frit	Bonded, Hermetic	10.1
G-6	16	360	Pyrex, Schott glass frit	Bonded, Hermetic	6.4
G-7	22	180	Pyrex, Schott glass frit	Bonded, Hermetic	
G-8	16	780	Pyrex, Schott glass frit	Open Air, Not Hermetic	8.8
G-9	32	150	Pyrex, Schott glass frit	Open Air, Hermetic	9.8
G-10	32	210	Pyrex, Schott glass frit	Open Air, Sample Slipped, Hermetic	
G-11	32	210	Pyrex, Schott glass frit	Open Air, Hermetic	6.1
G-12	40	90	Pyrex, Schott glass frit	Open Air, Hermetic	
G-13	40	75	Pyrex, Johnson Matthey Frit	Open Air, Not Hermetic	
G-14	32	86	Pyrex, Johnson Matthey Frit	Open Air, Not Hermetic	5.7
G-15	32	120	Pyrex, Johnson Matthey Frit	Open Air, Not Hermetic	
G-16	50	70	Pyrex, Schott glass frit	Open Air, Hermetic	5.3
G-17	50	70	Pyrex, Schott glass frit	Open Air, Hermetic	
A-1	30	300	Al_2O_3-Al_2O_3, Ticusil	Bonded - Not Hermetic	
A-2	32	330	Al_2O_3-Al_2O_3, EZ Flo 45	Not Bonded	
A-3	35	600	Al_2O_3-Al_2O_3, EZ Flo 45	Not Bonded	
A-4	32	360	Cermet-Al_2O_3, Cusil ABA	Bonded, Hermetic	67.6
A-5	32	480	Cermet-Al_2O_3, Cusil ABA	Bonded, Hermetic	
A-6	32	300	Cermet-Al_2O_3, Cusil ABA	Bonded, Not Hermetic	
A-7	32	420	Al_2O_3-Al_2O_3, Cusil ABA	Dirty Heat Shield, Bonded, Not Hermetic	
A-8	32	360	Al_2O_3-Al_2O_3, Cusil ABA	Bonded, Hermetic	
A-9	32	300	Cermet-Al_2O_3, Ticusil	Bonded, Not Hermetic	
A-10	25	360	Cermet-Al_2O_3, Cusil ABA	Bonded, Not Hermetic	73.9
A-11	25	423	Cermet-Al_2O_3, Cusil ABA	Bonded, Not Hermetic	62.1
A-12	25	500	Cermet-Al_2O_3, Cusil ABA	Bonded, Hermetic	82.9
A-13	38	170	Cermet-Al_2O_3, Cusil ABA	Bonded, Hermetic	118.9
A-14	38	300	Cermet-Al_2O_3, Cusil ABA	Bonded, Hermetic	
A-15	35	600	Al_2O_3-Al_2O_3, Cusil ABA	Air, Not Bonded, Not Hermetic	
A-17	70	100	Al_2O_3-Al_2O_3, Cusil ABA	Controlled cool-down, Bonded, not Hermetic	
	20	100			
A-18	70	60	Al_2O_3-Al_2O_3, Cusil ABA	Lid cracked, suspected from previous damage.	
A-19	70	70	Al_2O_3-Al_2O_3, Cusil ABA	Controlled power to maintain constant T after melt	
	25	40		Bonded, not Hermetic	
	30	60			
A-20	70	70	Al_2O_3-Al_2O_3, Cusil ABA	maintain constant T after melt	5.9
	30	100		Bonded, not Hermetic	
KA-1	38	280	Al_2O_3 on Kovar, Incusil ABA	Bonded,	
KA-2	38	250	Al_2O_3 on Kovar, Incusil ABA	Bonded, Hermetic	
KA-3	38	190	Al_2O_3 on Kovar , Incusil ABA	Bonded, Hermetic	
			Kovar on Al_2O_3, Incusil ABA	Bonded, Not Hermetic	

Table A.3 Coupon Test Summary

Expt. No.	Beam rep rate (Hz)	Time (sec)	Materials Combo.	Braze	Comments	Ultra. exam	Shear Strength (MPa)
17-2	8	313	Si-coated Si_3N_4	Ticusil			> 185
17-3	8	313	Si_3N_4 to Si_3N_4	Ticusil			>160
18-1,2	8	375	Si_3N_4 to Si_3N_4	Ticusil			87.5
18-3	8	313	Si_3N_4 to Si_3N_4	Ticusil	Offset	Good	
19-1	8	375	SiC to SiC	Ticusil	Offset	Bad	
19-2	8	375	SiC to SiC	Ticusil		.	1.6
20-1	8	313	Al_2O_3 to Al_2O_3	Ticusil	Crooked	Good	
20-9	12	83	Al_2O_3 to Al_2O_3	Ticusil			220
20-10	16	31	Al_2O_3 to Al_2O_3	Ticusil	Braze unmelted.	Good	
20-11	16	39.8	Al_2O_3 to Al_2O_3	Ticusil		Good	
21-1	8	313	cermet-cermet	Ticusil	Crooked	OK	
22-1	8	313	cermet on Al_2O_3	Ticusil	Crooked	Good	
22-2	8	375	cermet on Al_2O_3	Ticusil	Crooked		180
23-1	8	500	cermet on Al_2O_3	Nioro ABA	Incomplete melt.	Bad	.
23-2	8	563	cermet on Al_2O_3	Nioro ABA	Incomplete melt.		176
24-2	2	200	Glass on glass	Schott frit			
24-3	8	50	Glass on glass	Schott frit	Top glass cracked		
SN-1 (4 pieces)	70	10	Si_3N_4 to Si_3N_4	Cusil ABA			231 106 93 **143.3**
SN-3 (3 pieces)	70	5	Si_3N_4 to Si_3N_4	Cusil ABA			130 66 **98**
SN-4 (4 pieces)	90	10	Si_3N_4 to Si_3N_4	Cusil ABA			79 104 53 **78.7**
SN-5 (4 pieces)	90	8.5	Si_3N_4 to Si_3N_4	Incusil ABA			12 133 61 **68.7**
SN-6 (3 pieces)	90	5	Si_3N_4 to Si_3N_4	Incusil ABA			173 28 **100.5**
SN-7	90	15	Si_3N_4 to Si_3N_4	Cusil ABA	12 mm depth		
SN-8	90	12	Si_3N_4 to Si_3N_4	Cusil ABA	12 mm depth		163
SN-9	90	11	Si_3N_4 to Si_3N_4	Incusil ABA	12 mm depth		
SC-1 (2 pieces)	100	9	SiC on SiC	Incusil ABA	Poorly aligned.		
SC-2 (3 pieces)	120	7	SiC on SiC	Incusil ABA	One piece broke off or didn't bond.		
SC-3 (2 pieces)	90	12	SiC on SiC	Cusil ABA			78
SC-4 (2 pieces)	90	15	SiC on SiC	Ticusil			31
SC-5 (2 pieces)	90	15	SiC on SiC	Ticusil			
SC-Ti1	90	13	SiC on SiC	Ticusil	Ti interlayer		61
SC-Ti2 (3 pieces)	90	15	SiC on SiC	Ticusil	Ti interlayer		
SN-Ti1	90	14	Si_3N_4 to Si_3N_4	Ticusil	Ti interlayer		7
SN-Ti2	90	14	Si_3N_4 to Si_3N_4	Ticusil	Ti interlayer		

Table A.4
Tensile Test Sample Summary

Tensile Testing Samples					Cusil ABA	mils
I. D.	Freq, (Hz)	Time, (sec)	Hermeticity	Strength (MPa)	Ultrason	Remarks
T-1	60	80	leak	12.3	med	rc+mc
T-2	60	120	leak	71.9	strong	rc+mc+sma
T-3	60	150	leak	79.9	strong	rc
T-4	60	90	leak	25.7	strong	rc+mc
T-5	60	150	leak	64.4	med	rc+mc
T-6	60	120	leak	41.5	med	rc+mc
T-7	38	100	leak	4.8	weakest	rc+mc
T-8	38/20	100/100	pass	21.8	med	mc
T-9	38/20	100/150	pass	17.6	week	mc
T-10	38/20	100/150	pass	0.0		micro. study
T-11	38/20	100/150	pass	16.3		sma
T-12	38/20	100/150	pass	15.4		sma
T-13	38/20	100/100	pass	8.8		ma
T-14	50	200	leak	59.3	strong	rc+braze failure
T-15	45	220	leak	51.0	strong	rc+creamic failure
T-16	38/22/20	100/220/235	pass	49.5	strong	braze failure
T-17	38/22/20	100/100/300	pass	44.6	strong	braze failure+sma
T-18	50/25/20	80/20/200	leak	0.0	med	rc+ma: micro. study
T-19	45/25/20	85/20/195	pass	32.5	strong	ceramic failure+sma
T-20	38/22/20	100/100/300	pass	44.4	strong	ceramic failure+sma
T-21	38/22/20	100/100/198	pass	11.1	weak	ceramic failure+sma
T-22	38/22/20	100/100/131	pass	9.9	weakest	ceramic failure
T-23	38/22/20	100/100/300	pass	51.2	med	braze failure+sma
T-24	45/25/20	85/20/300	pass	42.4	med	braze failure
T-25	45/25/20	85/20/400	pass	50.0	med	ceramic failure+sma
T-26	50/45/20	40/40/370	pass	57.5	strong	braze+ceramic failure+sma
T-27	60/45/25/20	40/30/20/195	pass	0.0	med	ma: micro. study
T-28	60/45/25/20	40/30/20/240	pass	13.7	strong	braze failure+ma
T-29	40/60/40	30/70/100	leak	86.7		2rc + 7 cracks close to braze line
T-30	40/60/40	30/70/100				fogot to rotate sample
T-31	40/60/40	30/70/100				sample shattered/beam misaligned
T-32	40/50/40	30/70/100				sample shattered/beam misaligned
T-33	40/50/40	30/70/100	leak	85.4		rc + 7 cracks close to braze line
T-34	40/50/40	60/80/60	leak	78.4		rc + 8 cracks close to braze line
T-35	40	128				Sample worked off alignment
T-36	40	300	leak	82.2		rc + 7 cracks close to braze line
T-37	40/30	120/280	leak	84.9		7 cracks close to braze line
T-38	40/30/25	120/230/150	leak	91.4		8 cracks close to braze line
T-39	40/30/25	120/81				Sample worked off alignment
T-40	40/30	120/38	> 8X10^-5	22.9		7 cracks close to braze line +ma

T-41	40/30	120/230	>2X10^-5	77.9		1 crack close to braze line
T-42	30	450	Pass	60.0		no cracks + ma
T-43	35/40/20	100/100/50				3 mil,beam misaligned, worked off
T-44	30/40/20	100/100/50				3 mil, sma, no cracks, micro study
T-45	30/40/20	100/100/50		57.8		2 mil, Radial cracks on both sides
T-46	30/40/30/25/20/10	100/50/200/100/50/50		85.8		2 mil, no cracks, **joint didn't fail**
TB1	Standard brazing/baseline		pass	97.7	strong	Micro. Study
TB2	Standard brazing/baseline		pass	84.3	strong	
TB3	Standard brazing/baseline		pass	97.8	strong	
T49	40	100	NDL (pass)	10.8		ma
T50	30/40/30/25/20/10	100/50/200/100/50/50	NDL (pass)	0.0		sma + micro. study
T51	30/40/30/25/20/10	100/50/200/100/50/50	NDL (pass)	75.3		
T52	38/45/30	100/85/200	NDL (pass)	92.4		sma
T53	38/45/30/15	100/85/50/50	gross leak	65.3		sma + radical cracks on both sides
T54	38/45/30/15	100/85/50/50	gross leak	0.0		ma + mc +radical cracks+micro study
T55	30/40/30/25/20/10	100/50/200/100/50/50	1.5 X 10^-6	78.2		Motor power supply blow
T56	30/40/30/25/20/10	100/50/100/50/50/50	gross leak	55.4		radial cracks
T57	60/45/25/20	40/30/20/240	NDL (pass)	64.2		(same as T28, strength repeat)
T58	40	100	NDL (pass)	0.0		nice looking for display

NDL (pass) < 1 X10^-9cc/sec)

Notes:
ma: misalignment
mc: micro cracking

6. References

1. J. A. Halbleib, R. P. Kensek, G. D. Valdez, S. M. Seltzer, and M. J. Berger, 1992, "ITS: The Integrated TIGER Series of Electron/Photon Transport Codes - Version 3.0," *IEEE Transactions of Nuclear Science*, Vol. 39, pp. 1025-1030.
2. M.J Berger, 1963, "Monte Carlo Calculation of the Penetration and Diffusion of Fast Charged Particles," in *Methods in Computational Physics*, Vol. 1, Academic, New York.
3. D. Gartling, and R. Hogan, 1994, *Coyote II - A Finite Element Computer Program for Nonlinear Heat Conduction Problems, Sandia Report SAND-1179*, Sandia National Laboratories, Albuquerque, NM.
4. American Society for Testing and Materials, "Standard Test Method for Tension and Vacuum Testing Metallized Ceramic Seals," ASTM F 19-64, 1995.

DISTRIBUTION

Unclassified Unlimited Release

1	MS 9018	Central Technical Files, 8940-2
5	MS 0899	Technical Library, 4916
2	MS 0619	Review & Approval Desk, 12690 for DOE/OSTI for DOE/OSTI

Internal Distribution

1	MS 0188	C. E. Meyers, 4523
1	MS 0367	B. K. DamKroger, 1833
1	MS 0367	J. J. Stephens, Jr., 1833
2	MS 0367	S. J. Glass, 1833
1	MS 0367	T. B. Crenshaw, 1833
1	MS 0515	F. M. Bacon, 1561
1	MS 0516	G. L. Laughlin, 1564
1	MS 0516	C. N. Busick, 1564
1	MS 0516	J. P. Brainard, 1564
1	MS 0516	G. W. Smith, 1564
1	MS 0521	T. J. Young, 1567
1	MS 0615	H. J. Gieske, 9752
2	MS 0835	T. E. Voth, 9113
1	MS 0869	W. E. Packer, Sr., 14404
1	MS 0872	O. L. Butler, 14300
1	MS 0873	D. J. Malbrough, 14402
1	MS 0953	W.E. Alzheimer, 1500
1	MS 0953	T. J. Cutchen, 1501
1	MS 0958	G. A. Pressly, 1484
1	MS 0959	C. A. Walker, 1471
5	MS 0959	F. P. Gerstle, Jr., 1492
5	MS 0959	P. Yang, 1492
1	MS 0959	R. L. Poole, 1471
1	MS 0959	R. H. Moore, 1492
1	MS 0960	J. Q. Searcy, 1400
1	MS 0961	J. M. Harris, 1404
1	MS 1134	J. B. Kelley, 1846
2	MS 1179	J. A. Halbleib, Sr., 9341
20	MS 1182	B. N. Turman, 9521
1	MS 1188	R. A. Hamil, 9512
1	MS 1190	D. L. Cook, 9500
1	MS 1191	J. P. Quintenz, 9500
1	MS 1233	J. B. Woodard, 5131
1	MS 1349	R. E. Loehman, 1808
1	MS 1405	R. P. Goehner, 1822
2	MS 1405	B. B. McKenzie, 1822
1	MS 1411	M. F. Hosking, 1833
1	MS 1411	F. G. Yost, 1841
1	MS 1434	G. E. Pike, 1802
1	MS 1435	D. E. Arvizu, 1800
1	MS 1435	M. J. Cieslak, 1860